

# Numerical Simulation and Experimental Verification of Dry Pressed MgTiO<sub>3</sub> Ceramic Body during Pressureless Sintering

**Jiang Wang**

Wuhan University of Technology

**Yu Ni**

Wuhan University of Technology

**Kai Liu** (✉ [jiang608@qq.com](mailto:jiang608@qq.com))

Wuhan University of Technology

**Yanying Du**

Wuhan University of Technology

**Wei Liu**

Wuhan University of Technology

**Zijian Wang**

Huazhong University of Science and Technology - Main Campus: Huazhong University of Science and Technology

**Shangyu Huang**

Wuhan University of Technology

**Huajun Sun**

Wuhan University of Technology

---

## Research Article

**Keywords:** Pressureless Sintering, Numerical Simulation, MgTiO<sub>3</sub>, SOVS Model, Densification

**Posted Date:** January 15th, 2021

**DOI:** <https://doi.org/10.21203/rs.3.rs-143548/v1>

**License:** © ⓘ This work is licensed under a Creative Commons Attribution 4.0 International License.

[Read Full License](#)

---

# **Numerical Simulation and Experimental Verification of Dry Pressed MgTiO<sub>3</sub> Ceramic Body during Pressureless Sintering**

Jiang Wang<sup>b</sup>, Yu Ni<sup>b</sup>, Kai Liu<sup>\*a,b</sup>, Yanying Du<sup>c</sup>, Wei Liu<sup>b</sup>, Zijian Wang<sup>d</sup>, Shangyu Huang<sup>b</sup>, Huajun Sun<sup>\*a</sup>

a State Key Laboratory of Silicate Materials for Architectures, Wuhan University of Technology, Wuhan 430070, People's Republic of China

b School of Materials Science and Engineering, Wuhan University of Technology, Wuhan 430070, People's Republic of China

c School of Logistics Engineering, Wuhan University of Technology, Wuhan 430070, People's Republic of China

d State Key Laboratory of Materials Processing and Die & Mould Technology, School of Material Science and Engineering, Huazhong University of Science and Technology, Wuhan 430074, China

\*Corresponding author: E-mail address: liukai19870222@163.com (K. Liu)

174051406@qq.com (HJ.Sun)

## **Abstract**

To clarify the densification law of dry pressed MgTiO<sub>3</sub> ceramic body during pressureless sintering, SOVS model modified with creep characteristics was embedded into finite element software Abaqus. The selected model can effectively express the grain boundary characteristics and densification mechanism. The change law of relative density, shrinkage rate, sintering stress and grain size of MgTiO<sub>3</sub> cylindrical specimens were investigated by the above numerical simulation method. It

showed that the average relative density of ceramic body rose from 60% to 97% and the shrinkage rate respectively reached 17.28% and 11.99% in axial and radial direction. The average grain size increased from 1 $\mu\text{m}$  to 6  $\mu\text{m}$ . In order to verify the accuracy of the simulation results, corresponding sintering experiments on cylindrical specimens were carried out to obtain actual sintering densities and shrinkage rates. It showed that the errors of relative density and shrinkage is below 5% and 2%. Grain growth trend was also basically consistent with the simulation results. After that, the above numerical simulation method was applied into the prediction of fabricating MgTiO<sub>3</sub> filter with complex structure. Therefore, the present work provided a reliable numerical simulation method to predict the densification behavior of MgTiO<sub>3</sub> ceramics during the pressureless sintering process, which was helpful to design and fabricate microwave dielectric products.

**Key words:** Pressureless Sintering; Numerical Simulation; MgTiO<sub>3</sub>; SOVS Model; Densification;

## 1 introduction

MgTiO<sub>3</sub> is a kind of microwave dielectric ceramics with excellent dielectric and mechanical properties, which is widely used in the fields of ceramic capacitors, microwave antennas, filters and ceramic substrate[1]. Due to the complex structure with holes and grooves, the MgTiO<sub>3</sub> wave filter was usually processed by CNC machining in the past. But due to the high hardness and brittleness of ceramics, CNC method has some limitations on fabricating MgTiO<sub>3</sub> components, which hinder further design and development of filter products. In recent years, it was a trend to fabricate MgTiO<sub>3</sub> wave filter via dry pressing combined with pressureless sintering. The process of pressureless sintering could decrease the porosity of MgTiO<sub>3</sub> green bodies[2]. However, because it is difficult to predict and control the densification behavior of ceramics during sintering, large sintering defects and low yield are the

main problems in MgTiO<sub>3</sub> filter production [3~4]. It can reduce the number of trial and error and production cost to analyze the ceramic sintering process using numerical simulation method.

The powder model for numerical simulation has been developed for more than ten years[6]. Ashby combined pore movement and surface tension to establish the constitutive model basis for powder sintering[7]. Coble further studied the change rules of pore and grain microstructure and optimized the sintering process[8]. Riedel adopted hexagonal grain as the microscopic model and deduced a series of constitutive models [9]. Cocks proposed the theory of creep and grain boundary diffusion [10]. The rheological model known as SOVS model proposed by Skorohod and modified by Olevsky has been mainly applied [11]. Kraft summarized the rheological theory and simulated the solid-phase sintering of SiC ceramics [12].

Recently, SOVS model has been developed and applied. WANG simulated the solid phase sintering of alumina ceramics using the improved SOVS model, and the simulation results were consistent with the actual sintering [13-14]. Hong simulated the sintering of iron powder under the condition of fully considering the influence of heat conduction, thermal convection, thermal radiation and thermophysical parameters[15]. Anastasiia study the field assisted sintering of silicon germanium alloys by a finite element method[16]. YANG simulated the sintering of Li metal at different temperatures and considered the three stages of sintering[17].

Previous studies have proved the feasibility of SOVS model, which has the advantages of simple parameters and easy measurement. But most of the existing researches only focus on deformation, the relative density changes and grain growth during simulation are rarely studied. Furthermore, the previous studies mostly ignored the thermal expansion and creep behavior. Thermal expansion affects the deformation at the initial stage of sintering[13]. In addition, there is no research about the simulation of MgTiO<sub>3</sub> wave dielectric ceramics. Therefore, it is necessary to use SOVS model modified with creep characteristics to simulate the sintering

densification process of MgTiO<sub>3</sub> filter with complex structure.

In this study, SOVS model modified with creep characteristics was embedded into finite element software to simulate pressureless sintering process of MgTiO<sub>3</sub> in Abaqus. The changing law of relative density, shrinkage, sintering stress and grain growth along sintering process was analyzed and experimentally verified. The densification behavior of MgTiO<sub>3</sub> wave filter was also predicted and verified during the pressureless sintering process, which was helpful to structure design and practical production of MgTiO<sub>3</sub> ceramic components.

## 2 Sintering model and parameter acquisition

### 2.1 Route planning

The flow chart of this work is shown in Figure 1.



FIG. 1 Flow chart of experiment

### 2.2 The Modified SOVS model

Skorohod-Olevsky Viscous Sintering model which is known as the SOVS model, is a continuous mechanical models based on the theory of porous plasticity and nonlinear viscoplastic deformation. In general, the SOVS constitutive relation of nonlinear porous materials can be expressed as:

$$\sigma_{ij} = 2\eta(\varphi\dot{\varepsilon}'_{ij} + \psi\dot{\varepsilon}\delta_{ij}) + PL\delta_{ij} \quad (1)$$

Where,  $\sigma_{ij}$  is cauchy stress tensor,  $\sigma(w)$  is equivalent stress,  $\dot{\varepsilon}'_{ij}$  is deviator

strain rate tensor,  $\dot{\epsilon}$  is trace of strain rate tensor, and  $\delta_{ij}$  is Kronecker coefficient.  $\varphi$  and  $\psi$  are the standardized shear viscosity and volume viscosity respectively. PL is the sintering stress,  $\eta$  is the shear viscosity of solid, and their definitions are as follows:

$$\varphi = (1 - \theta)^2 \quad (2)$$

$$\psi = \frac{2}{3} \cdot \frac{(1 - \theta)^3}{\theta} \quad (3)$$

$$P_L = \sigma_s = \frac{6\gamma_s}{G} (1 - \theta)^2 \quad (4)$$

$$\eta = \eta_0 \exp\left(\frac{Q_v}{RT}\right) \quad (5)$$

Where  $\theta$  is porosity,  $\gamma_s$  is specific surface energy, G is average grain size,  $Q_v$  is surface activation energy, R is gas constant, T is absolute temperature, and  $\eta_0$  is the initial shear viscosity of solid.

With the progress of sintering, grain boundary diffuses with temperature, so the grain size also increases. The growth rule described by Guillaume Bernard-Granger is as follows [16] :

$$G = \frac{G_0}{\sqrt{G_0 k_1 (\rho_0 - \rho) + 1}} \quad (6)$$

Where, G0 is the initial average grain size, which can be measured through the analysis of SEM images by image-Pro Plus software.  $k_1$  is a constant that does not change with temperature,  $\rho_0$  is the initial relative density, and  $\rho$  is the relative density that changes constantly during sintering.

Cocks defined the bulk expansion strain increment  $\Delta\bar{\epsilon}^{sw}$  and shear creep strain increment  $\Delta\bar{\epsilon}^{cr}$  during sintering, which were defined as follows:

$$\Delta\bar{\varepsilon}^{sw} = -\frac{p + \sigma_s}{2\phi\psi} \Delta t \quad (7)$$

$$\Delta\bar{\varepsilon}^{cr} = \frac{\tilde{q}}{3\phi\psi} \Delta t \quad (8)$$

Where, P is equivalent hydrostatic pressure, and  $\tilde{q}$  is mises equivalent deviator stress.

### 2.3 parameter acquisition

Owens two-liquid method was used to test specific surface energy of ceramics. bbV-1000 high temperature viscometer was used to test the viscosity-temperature curve of MgTiO<sub>3</sub> ceramics. The experimental results are synthesized into arrhenius function (5). NETZSCH LFA 457 MicroFlash laser thermal conductivity meter was used to test the thermal diffusion coefficient of MgTiO<sub>3</sub> ceramics (sample diameter: 12.5-12.7mm, thickness: 1-3mm). The specific values are shown in Table 1.

Table1

parameter	value
specific surface energy	34.7 mN/m
initial average grain size	0.5~2um
surface activation energy	2.73×10 <sup>5</sup> J/mol
initial shear viscosity	2.09×10 <sup>-8</sup> Gpa*s
Thermal conductivity	3.548~12.908W/m/K (199.7~1400°C)
specific heat capacity	1169700~1441000 J/g/K (199.7~1400°C)
gas constant	8.314J/(mol·K)

FORTTRAN-based Abaqus user subroutine can implement the constitutive model and parameter input. In this study, CREEP subroutine was adopted. Variables can be defined in subroutines, such as relative density, grain size, and so on.

## **2.4 The experiment**

Before sintering,  $\text{MgTiO}_3$  is formed by dry pressed. So the relative density distribution of the green body after dry pressed should be imported. This can be done by defining the initial relative density in the subroutine. Cylindrical sample with the radius of 5mm and the height of 10mm were prepared by pressing as standard samples. In the standard group, the powder particle size was 0.1mm, and the initial temperature was 20°C. The maximum sintering temperature reached 1350°C after 4.5h of continuous heating, and the holding time was 3h, and then the powder was naturally cooled to room temperature. Take 1/4 of the sample as the research object.

## **3 Results and discussion**

### **3.1 Simulation results**

The simulation results of relative density are shown in figure 2. Before the sintering, the relative density of each part of the dry pressed body was different. The average value is about 0.6, but the relative density around the top surface of the cylinder is relatively high, while the relative density around the bottom surface of the cylinder is relatively low. After sintering, the relative density of the center of the top surface is relatively low, while that of the center of the bottom surface is relatively high. The overall relative density rises from 0.6 to about 0.97.

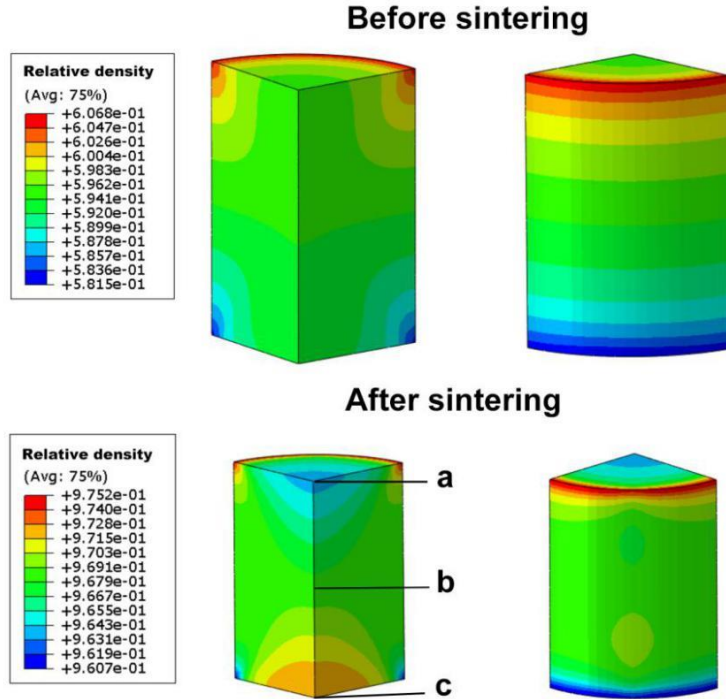


FIG. 2 Sintering simulation results of standard cylindrical sample

In figure 2, three points with large differences in relative density were selected, and their relative density change curves were shown in figure 3. In the early heating process, the relative density did not change. When the temperature is close to the sintering temperature (1350°C), the relative density begins to increase. After holding for a certain time, the relative density does not change and reaches the maximum value. For point A, B and C, before sintering, point A has the highest relative density and point C has the lowest. But after sintering, point A is the lowest and point C is the highest. The reason is that after pressing, the top surface, namely point A, contacts with the punch, so the pressing force is slightly higher than the rest surface, so the relative density is also higher. In simulation, the displacement along the Z direction is limited at the bottom of the sample, and the gravity load is applied. Therefore, the sintering stress is higher and the relative density is also higher.

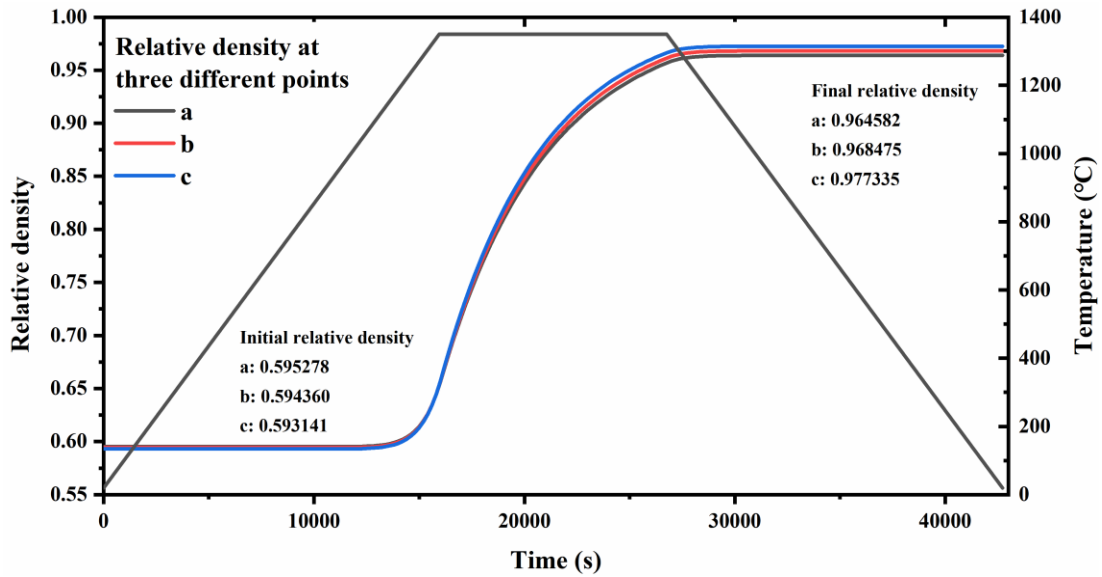


FIG. 3 Relative density change curve

Figure 4 shows the curve of size change and shrinkage rate change of sintering simulation. Both the radial and axial sizes increase slowly in early stage. At this point, the shrinkage rate is negative, that is, the sample volume has expanded. In the early stage of sintering, thermal expansion played a dominant role, and the thermal conductivity and thermal expansion coefficient of the material determined the volume change. With the temperature rising to 1350°C, the size of the sample decreases sharply, and the shrinkage rate is positive with the rapid growth rate. In this stage, the creep mechanism of sintering plays a leading role. Under the action of sintering stress, the sample begins to shrink, and the relative density also increases rapidly in this stage. Finally, the axial shrinkage rate was gradually greater than the radial rate, and finally reached 17.28%, while the radial rate was 11.99%. The reason is that axial gravity is added in the simulation process, and the axial shrinkage rate is higher under the action of gravity and sintering stress.

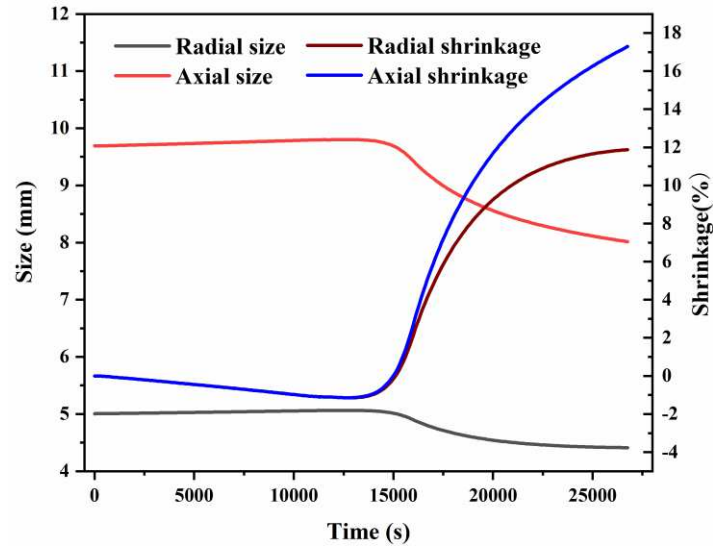


FIG. 4 Size and shrinkage change curve

Figure 5 shows the stress cloud map of each period of sintering. The external stress was higher than the internal stress at the beginning of sintering, which was the residual stress generated by pressing. As the temperature rises to 1350°C, the stress distribution is different, increasing from top to bottom, and finally forming stress concentration at the bottom center. The reason is that the constraint on the bottom surface to limit its displacement makes it lose the degree of freedom in the Z direction. Therefore, under the action of sintering stress, the stress accumulates downward and causes stress concentration. In the cooling stage of sintering, the stress concentration area is gradually eliminated, and the stress inside the sample block tends to be average. The surrounding area of the lower surface of the sample is slightly higher than other areas under the action of boundary conditions. Figure 6 shows the displacement (deformation) cloud diagram of the material after sintering. This diagram indicates the deformation direction of sintering densification, that is, shrinkage deformation is carried out from top to bottom and from outside to inside.

FIG. 5 MISES stress distribution diagram

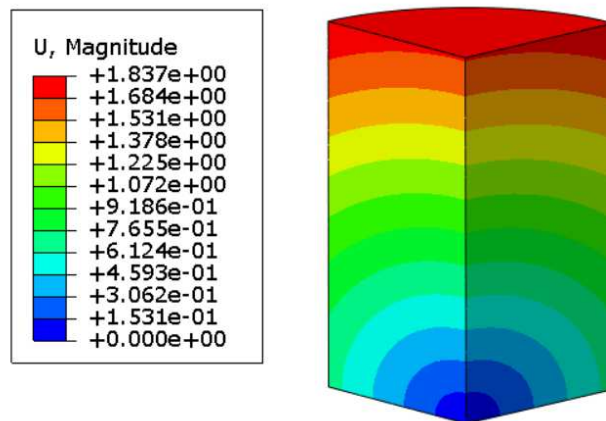


FIG. 6 Material displacement (deformation) distribution diagram

Figure 7 shows the simulated grain growth diagram. It can be seen that grain growth is closely related to the change of relative density. When the relative density is less than 80%, the grain growth is slow. When the relative density is greater than 90%, the grain growth is accelerated. Figure 8 shows the statistical graph of grain size after simulation. It can be seen from the figure that the size distribution is relatively concentrated, and the grain size increases from 0.001mm at the initial setting to 0.005867mm on average.

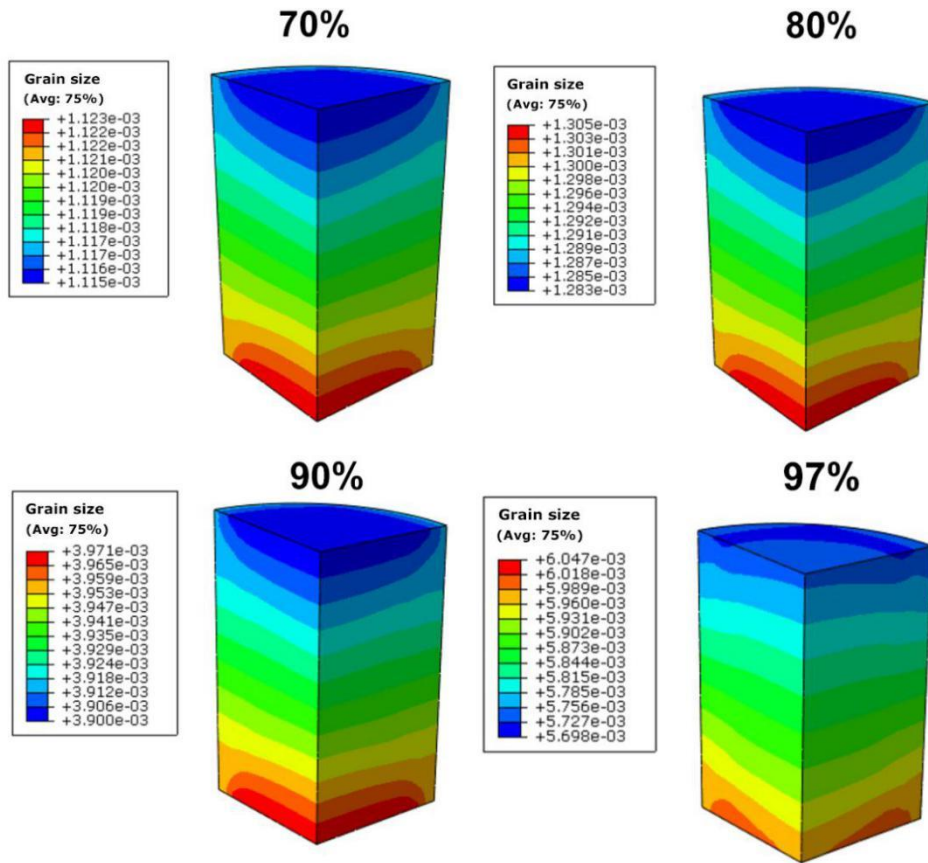


FIG. 7 Grain growth diagram

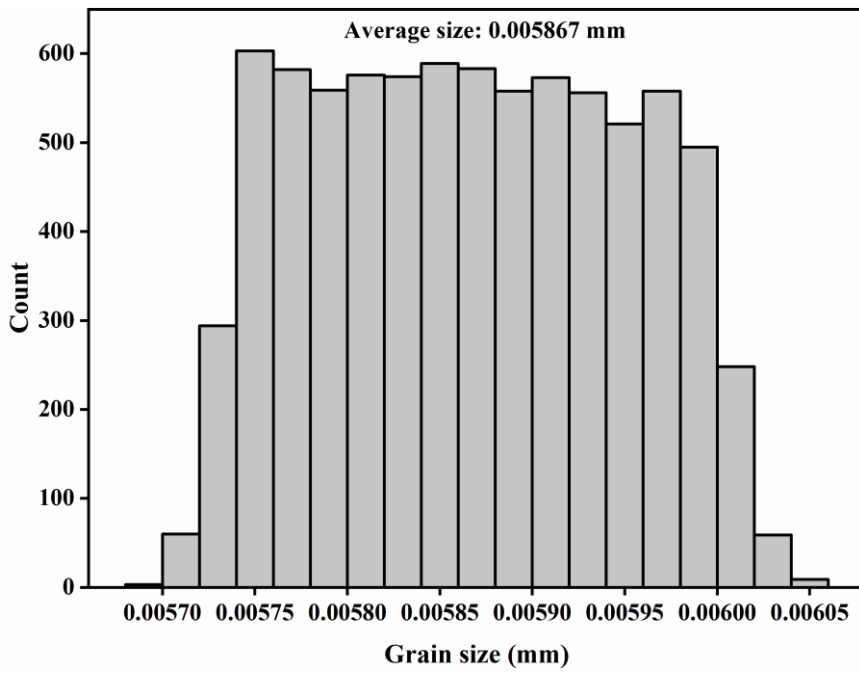


FIG. 8 Grain size statistics of sintering simulation

Pressureless sintering of ceramics is a very complex process, including the bonding stage, sintering neck growth stage and spheroidization stage. In the early stage of sintering, the sintering temperature is not high enough to provide sufficient activation energy for the sintered body. At this time surface diffusion is the main form of material diffusion. However, surface diffusion only changed the shape of pores between particles, but did not change the volume of pores, so the relative density of sintered body did not change. With the increase of sintering temperature, the temperature reaches the critical sintering temperature, and grain boundary diffusion becomes the main form of diffusion. As the sintering process goes on, particles accumulate and the contact area between particles increases. The grain boundary is formed gradually as the center distance approaches. At the same time, the shape of the hole will change, and the size of the hole will decrease. The connected macropores become isolated pores, and the pores gradually shrink until most or all of them are eliminated from the crystal. When the density of the body is low, the number of grain boundaries is small, so the grain growth rate is slow. When the density is higher, the grain boundary is more, so the grain grows faster.

## **3.2 Experimental Verification**

### **1) Relative density**

The dielectric property and quality factor of  $\text{MgTiO}_3$  depend on its density. So the change of relative density is the focus of the research. Figure 9 shows the cylinder samples which was equally cut into three parts along the height direction. The relative densities of the three parts were measured and compared with the simulated values. The results were shown in Table 2. The distribution of the relative density of the simulated values is consistent with the actual measurement, and the errors of the three parts are all within 5%. The error is caused by the difference between the material defined by the simulation and the actual material. In the simulation, we mainly defined the thermodynamic properties of materials. The actual material is more complex, which contain a small amount of additives such as burning AIDS.

FIG.9 Comparison of samples before and after sintering

Table2

	Simulation value	Actual value	Relative error
up	96.2%	92.1%	4.45%
middle	96.8%	92.3%	4.87%
down	97.4%	92.8%	4.90%

## 2) Size Change and Shrinkage

Figure 10 shows the shrinkage curve of simulation and actual sintering without considering gravity. The results of SOVS simulation are generally consistent with the trend of actual sintering. The difference is that the thermal expansion effect of the material is actually less pronounced than in the simulation. The sintering temperature of MgTiO<sub>3</sub> is set at 1350°C, but the actual maximum sintering temperature is only 1266.3°C. The reason is that the actual powder contains a small amount of impurities, which will be ignored in the simulation. The final shrinkage rate of both numerical simulation and practical sintering is about 14%. Table 3 shows the shrinkage ratio between simulated values and actual values. After sintering, both the simulated size and the actual size shrink, and the Z direction shrink more. The error is within 2%.

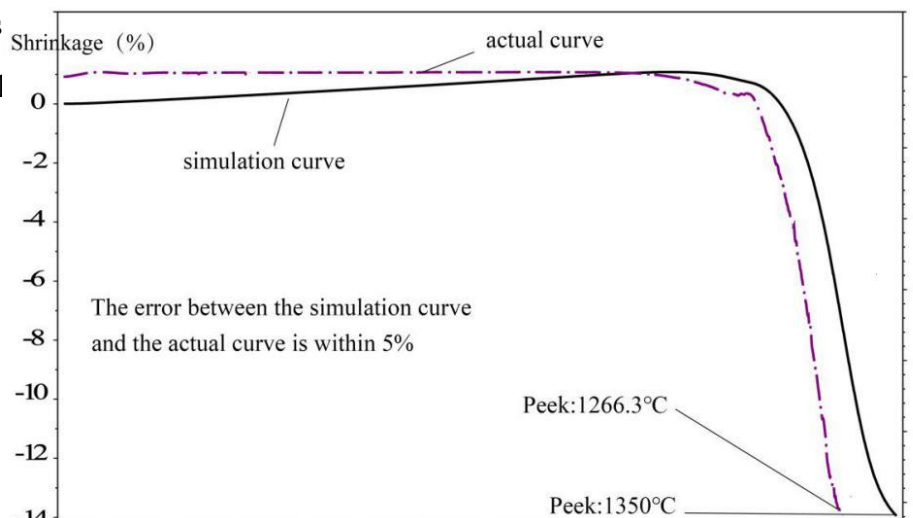
FIG. 10 Comparison curve of shrinkage change

Table3

	Initial body size	Sintering simulation size	Simulation shrinkage	Actual Sintering size	Actual shrinkage	Relative error
Axial	10	8.81	11.86%	8.66	13.36%	1.73%
Radial	10	8.27	17.30%	8.39	16.14%	1.43%

### 3) Grain size

Figure 11 is the SEM diagram of the sample. Before sintering, the gap between grains is large and the grains are independent. Three points in the sample were selected for SEM observation. After sintering, sintered neck was formed between grains and grain boundary was gradually form into a w



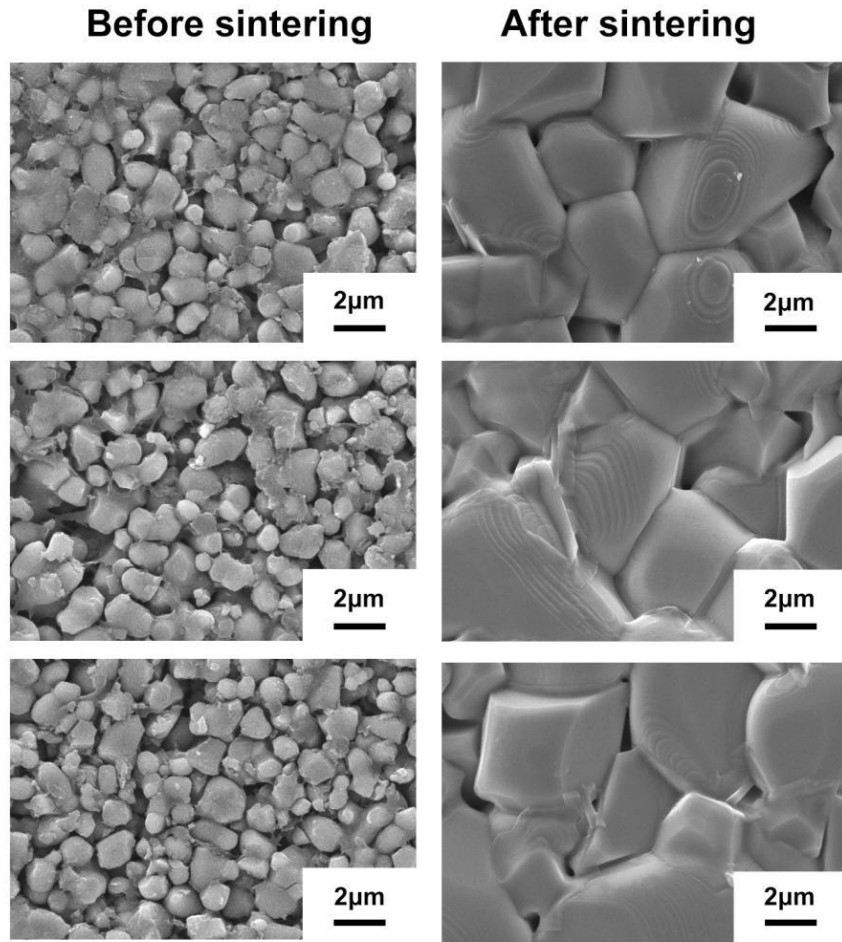


Fig. 11 SEM of grain size

By using IPP software to conduct particle size statistical analysis of SEM figures, figure 10 shows the statistical graph of grain size after actual sintering. It can be seen that the average grain size of the green body before sintering is 0.000988mm, while that after sintering is 0.00528mm. It can be seen that the distribution of grain size in actual sintering is wider and there are more abnormal growing grains. Compared with figure 8, simulation result is basically consistent with the actual result.

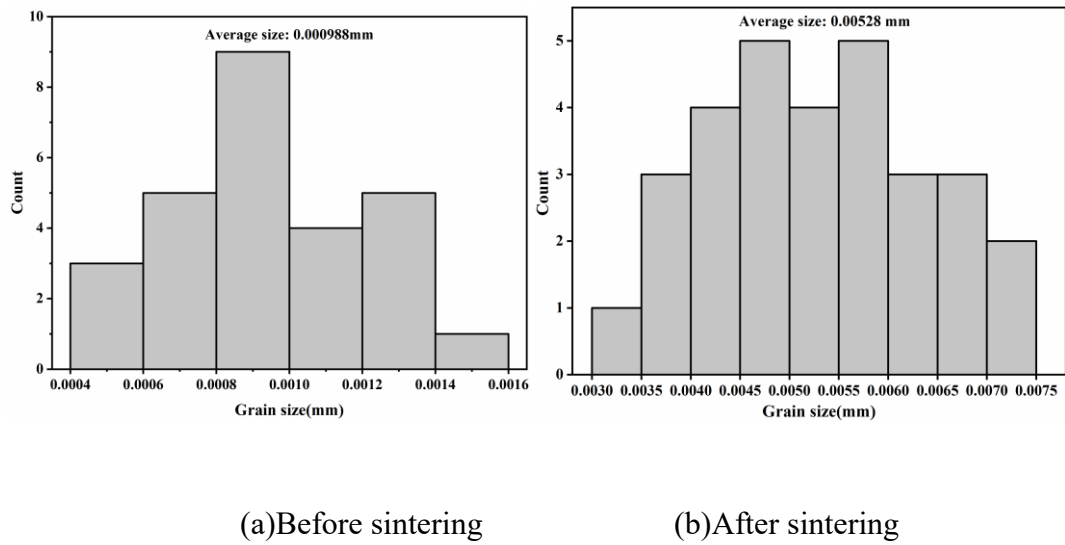


FIG. 12 Grain size statistics of actual sintering

### 3.3 Application on complex filter model

Figure 13 shows the MgTiO<sub>3</sub> ceramic filter with complex structure, which has more blind holes and grooves. The sintering model was used to simulate the densification process. The relative density at the bottom of the blind hole and the bottom of the groove are large, and the maximum value approaches 100%. The upper edge and groove edge of the blind hole are low, and the circular arc of groove edge is weak, with relative density only about 75%. Figure 14 shows the grain growth diagram. In the areas with high relative density, the gap between grains is small and the diffusion resistance is large, so the growth of grains is slow.

FIG. 13 Relative density distribution of filter

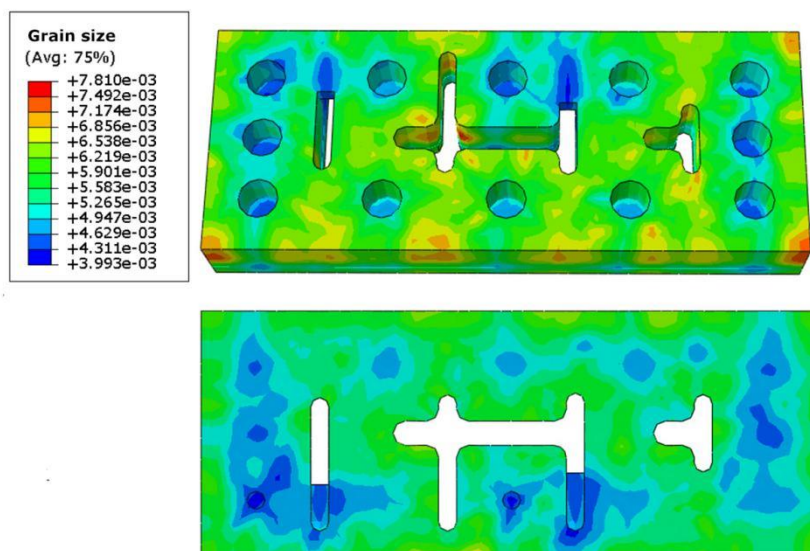


FIG. 14 Grain size distribution of filter

FIG. 15 shows the distribution of sintering stress, and three points are selected for analysis. Point A is the bottom of the blind hole, and the sintering stress is the largest, reaching about 6700Pa. Both Points B and C are side walls of the circular groove. However, the sintering stress at point B is the smallest, only about 3800Pa, while it is greater at point C. Point C is farther from the edge of the part and has a larger thickness. But point B is close to the edge, and it's thin. The driving force of

sintering in the thin-walled area is far less than that in the thick-walled area, so the sintering stress at point B is smaller and the relative density is also smaller.

The concave groove and blind hole with radian should be avoided as far as possible in the design of ceramic parts with complex structure. The depth of the groove should not be too large. Groove should be designed as close to the center of the part as possible, not as close to the edge.

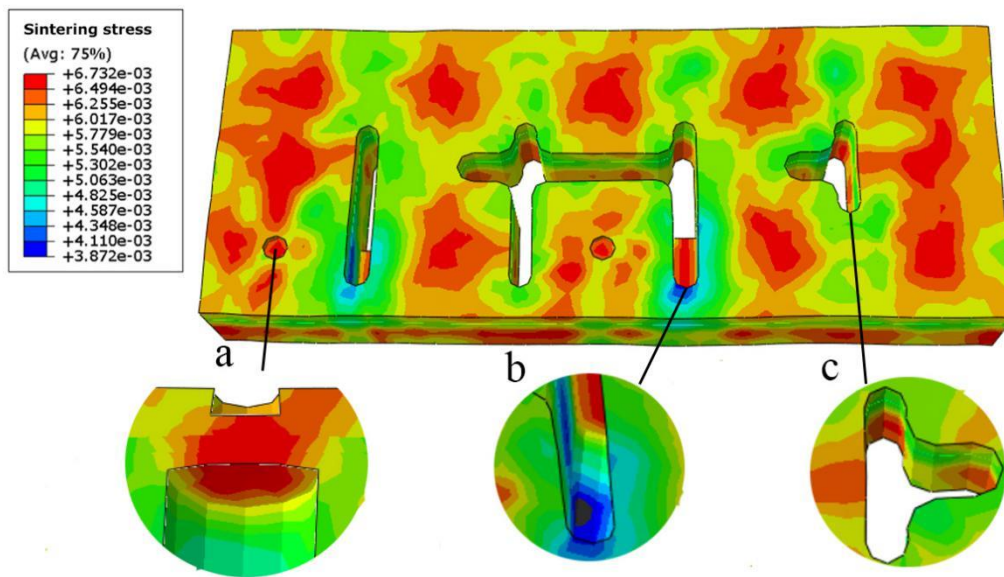


FIG. 15 Sintering stress distribution of filter

In order to verify the accuracy of complex shape sintering simulation, we cut the sintered parts and select four of them for relative density verification. As shown in figure 16. The verification results are shown in Table 4. The verification error is within 2%, which further explains the accuracy of the simulation.

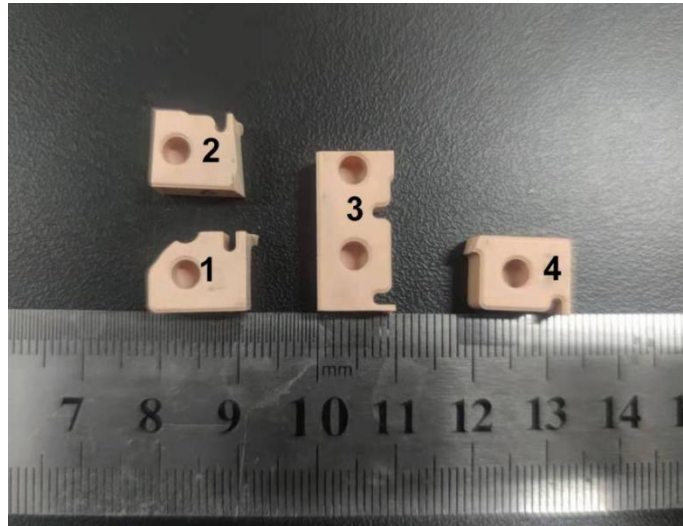


FIG. 16 The cut part of sintered part

Table 4

	Simulation value	Actual value	Relative error
1	93.81%	92.45%	1.50%
2	94.15%	94.63%	0.50%
3	94.57%	96.30%	1.90%
4	93.91%	95.53%	1.70%

## 4 conclusion

In this paper, pressureless sintering simulation of  $\text{MgTiO}_3$  ceramic body is studied, by embedding SOVS model modified with creep characteristics into finite element software Abaqus. The relative density, shrinkage, grain growth and sintering stress of were analyzed and experimentally vericated through cylindrical sample and complicated wave filter. It was concluded as below:

(1) Simulation results show that the average relative density rises from 60% to about 97%. The shrinkage rate resepectively reached 17.28% and 11.99% in axial and radial direction. The average grain size increased from 1 $\mu\text{m}$  to 6 $\mu\text{m}$ .

(2) Sintering experiments were carried out to obtain actual sintering densities and shrinkage rates. It showed that the errors of relative density and shrinkage is below 5% and 2%. Grain growth was also basically consistent with the simulation results.

(3) The method is used to simulate the filter with complex structure. The relative density and grain size were analyzed, which provides guidance for its practical production. The simulation results of complex shapes are verified, and the simulation error is within 2%.

### **Acknowledgements**

This work was supported by the National Natural Science Foundation of China (Grant Nos. U1806221, 51672198), Innovation and Development Project of Zibo City (2017CX01A022), Instruction & Development Project for National Funding Innovation Demonstration Zone of Shandong Province (2017-41-1, 2017-41-3, 2018ZCQZB01, 2019ZCQZB03), Central Guiding Local Science and Technology Development Special Funds (Grant Nos. 2060503), and Key Research & Design Program of Shandong Province (2019GGX102011).

[1] X. Su, G. Bai, J. Zhang, Preparation and flash sintering of MgTiO<sub>3</sub> nanopowders obtained by the polyacrylamide gel method, *Appl. Surf. Sci.* 442(2018) 12-19.

[2] L. He, H. Yu., M. Zeng, Phase compositions and microwave dielectric properties of MgTiO<sub>3</sub>-based ceramics obtained by reaction-sintering method, *J. Electroceram.* 40(2018)360–364.

[3] J. C. Maya, F. Chejne, S. K. Bhatia, Novel model for the sintering of ceramics with bimodal pore size distributions: Application to the sintering of lime, *Aiche. J.* 63(2017)894-902.

[4] Y. Wang, L. Y. Zhang, S. B. Zhang, Sintering behavior and microwave dielectric

properties of MgZrTa<sub>2</sub>O<sub>8</sub> ceramics with fluoride addition, *Mater. Lett.* 219(2018)233-235.

[5] C. Van Nguyen, S. K. Sistla, S. Van Kempen, A comparative study of different sintering models for Al<sub>2</sub>O<sub>3</sub>, *J. Ceram. Soc. Jpn.* 124(2016)301-312.

[6] P. Cao, C. Zhou, F. Jin, Tire–Pavement Contact Stress with 3D Finite-Element Model—Part 1: Semi-Steel Radial Tires on Light Vehicles, *J. Test. Eval.* 44(2016)788-800.

[7] F. Swinkels, M. Ashby, A second report on sintering diagrams, *Acta. Metal. Sin.* 29(1981)259-281.

[8] C. Hsueh, A. Evans, R. L. Coble, Microstructure development during final/intermediate stage sintering Pore/grain boundary separation, *Acta. Metal. Sin.* 30(1982)1269-1279.

[9] H. Riedel, J. Svoboda, A theoretical study of grain growth in porous solids during sintering, *Acta. Metal.* 41 (1993) 1929–1936.

[10] A. C. F. Cocks, The structure of constitutive laws for the sintering of fine grained materials, *Acta. Metal. Sin.* 42(1994) 2191-2210.

[11] M.W. Reiterer, K.G. Ewsuk, An Analysis of four different approaches to predict and control sintering, *J. Am. Ceram. Soc.* 92 (2009) 1419–1427.

[12] T. Kraft, H. Riedel, Numerical simulation of solid state sintering; model and application, *J. Eur. Ceram. Soc.* 24(2004) 345–361.

[13] Z. Wang, Y. Shi, W. He, Compound process of selective laser processed alumina parts densified by cold isostatic pressing and solid state sintering: Experiments, full process simulation and parameter optimization, *Ceram. Int.* 41(2015)3245-3253.

[14] Z. Wang, W. He, Y. Shi, Experimental based full process simulation of alumina selective laser processed parts densified by cold isostatic pressing and solid state

sintering, *J. Eur. Ceram. Soc.* 34(2014)1853-1863.

[15] H. He, J. Wang, J. S. Li, Z. Chen, J. Sun, Y. You, Temperature field simulation of powder sintering process with ansys, *IOP. Conf.* 324(2018)8-12.

[16] A. Tukmakova, A. Novotelnova, K. Samusevich, A. Usenko, D. Moskovskikh, A. Smirnov, Simulation of field assisted sintering of silicon germanium alloys, *MATERIALS.* 12(2019)570-583.

[17] L. Yang, X. Gan, C. Xu, C. L. Lang, Z. Jian, Molecular dynamics simulation of alloying during sintering of li and pb metallic nanoparticles, *Comp Mater Sci.* 156(2019) 47-55.

[18] G. Bernard-Granger, C. Guizard, New relationships between relative density and grain size during solid-state sintering of ceramic powders, *Acta Mater.* 56(2008) 6273–6282.

# Figures

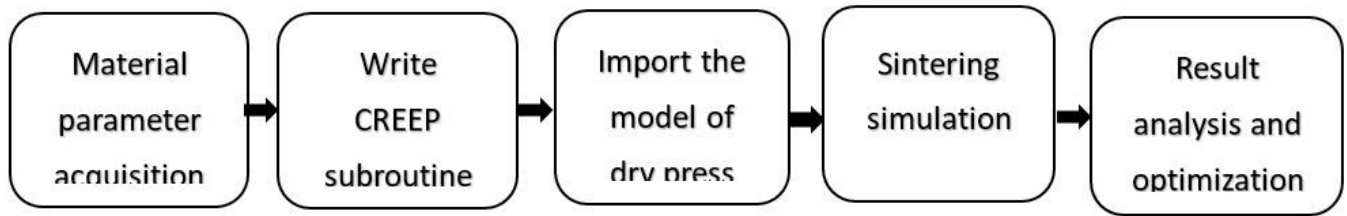


Figure 1

Flow chart of experiment

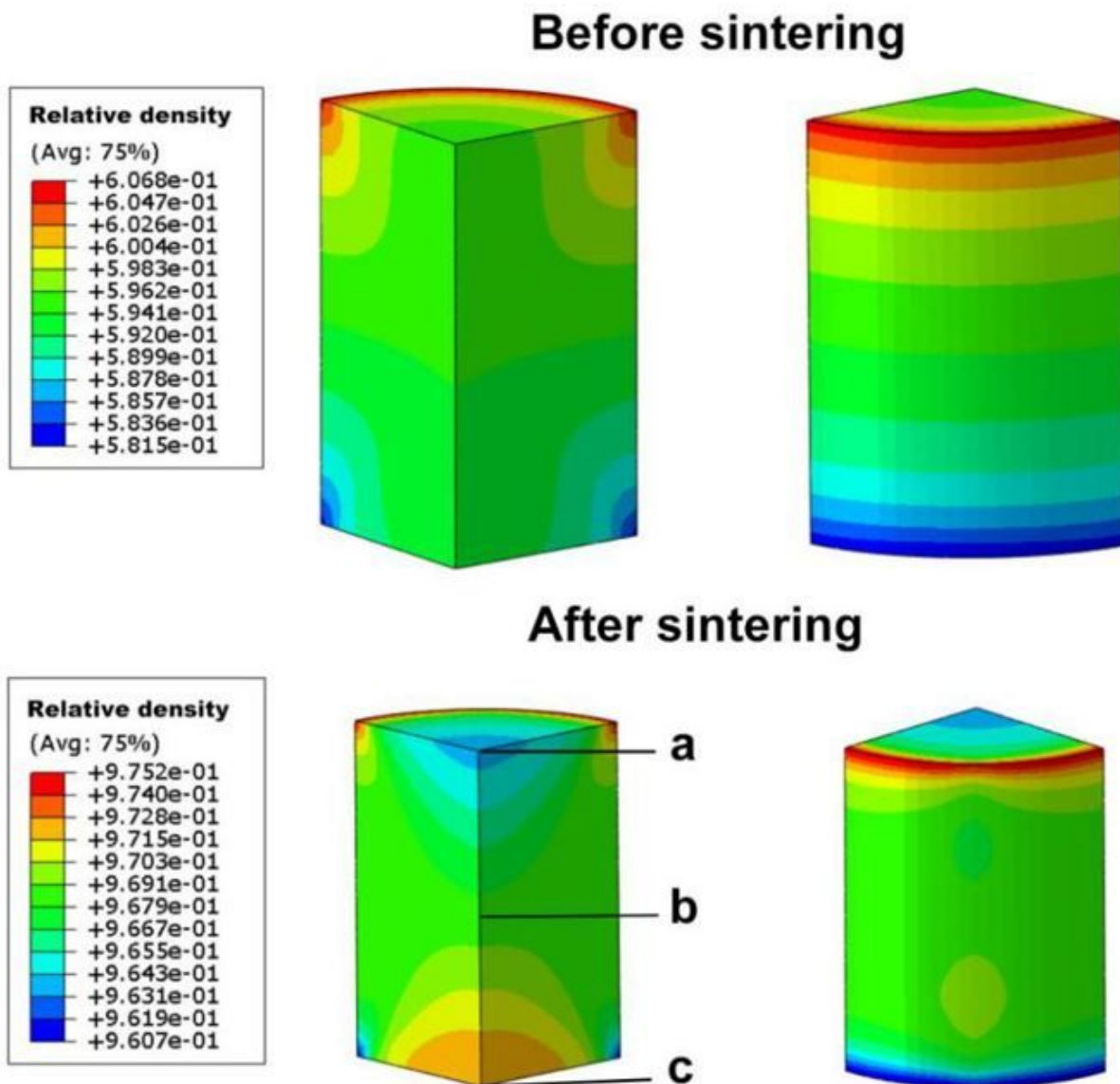


Figure 2

Sintering simulation results of standard cylindrical sample

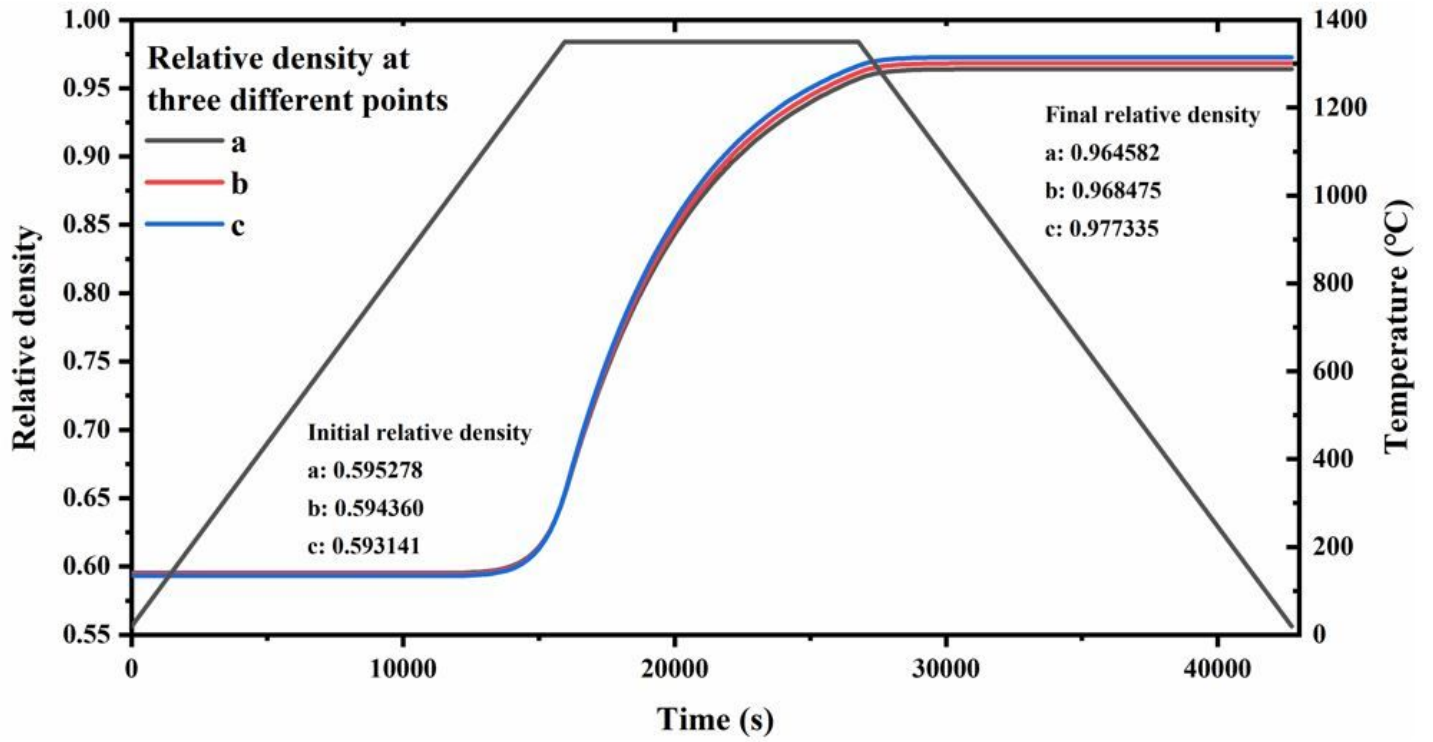


Figure 3

Relative density change curve

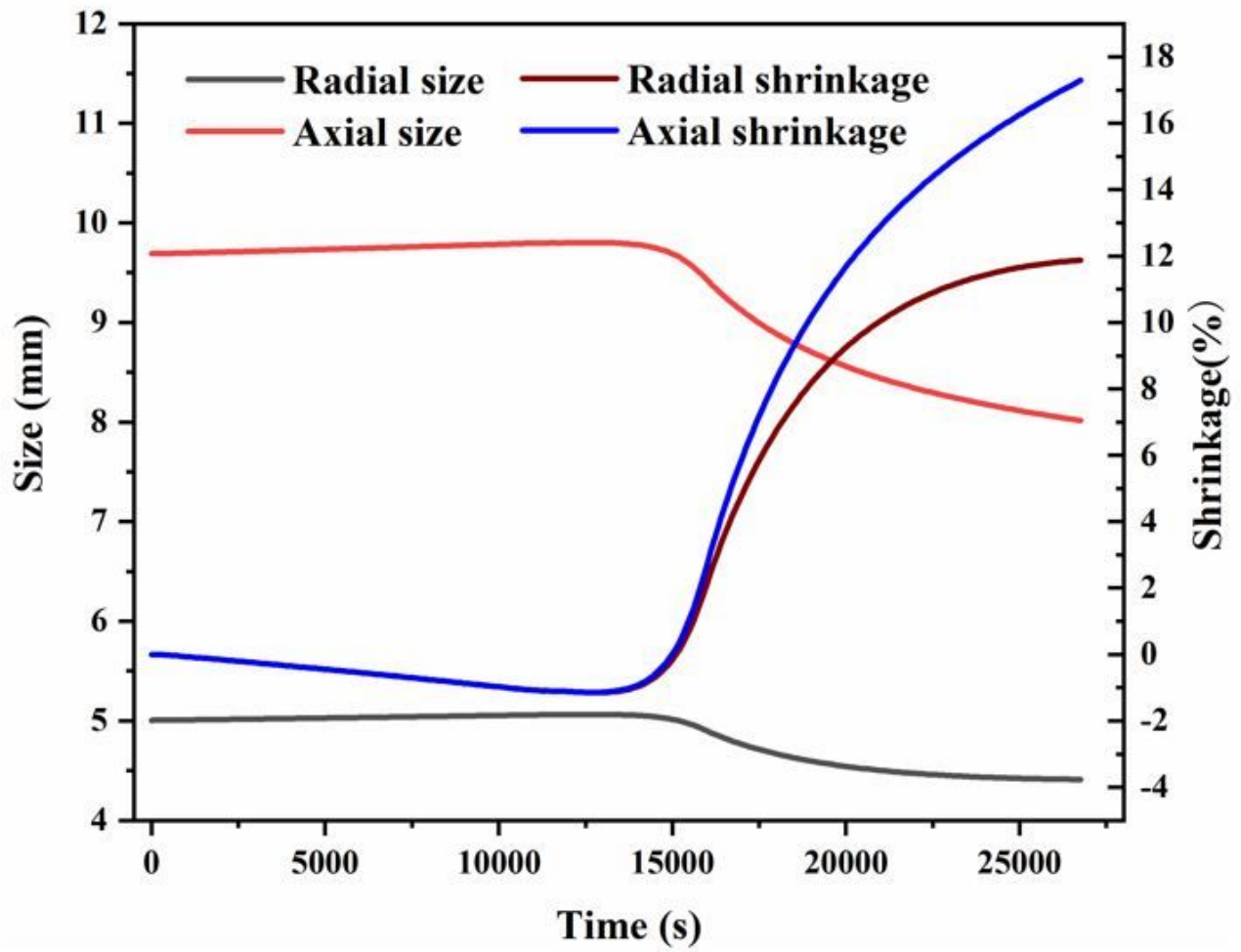


Figure 4

Size and shrinkage change curve

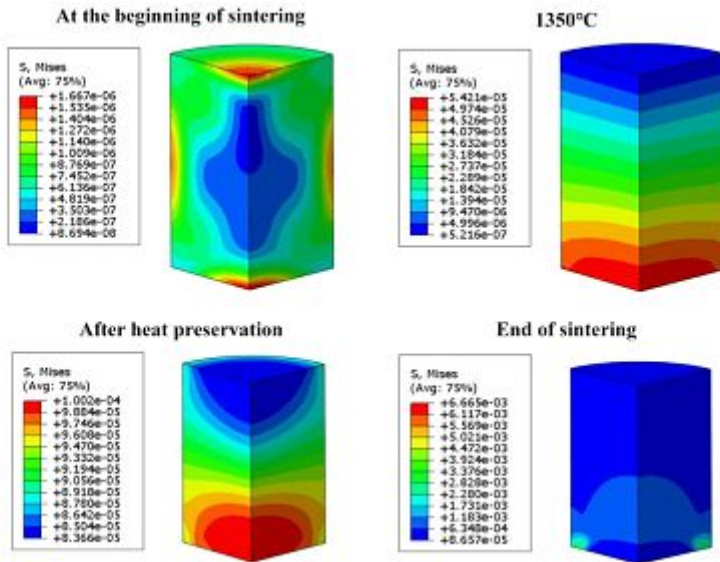


Figure 5

MISES stress distribution diagram

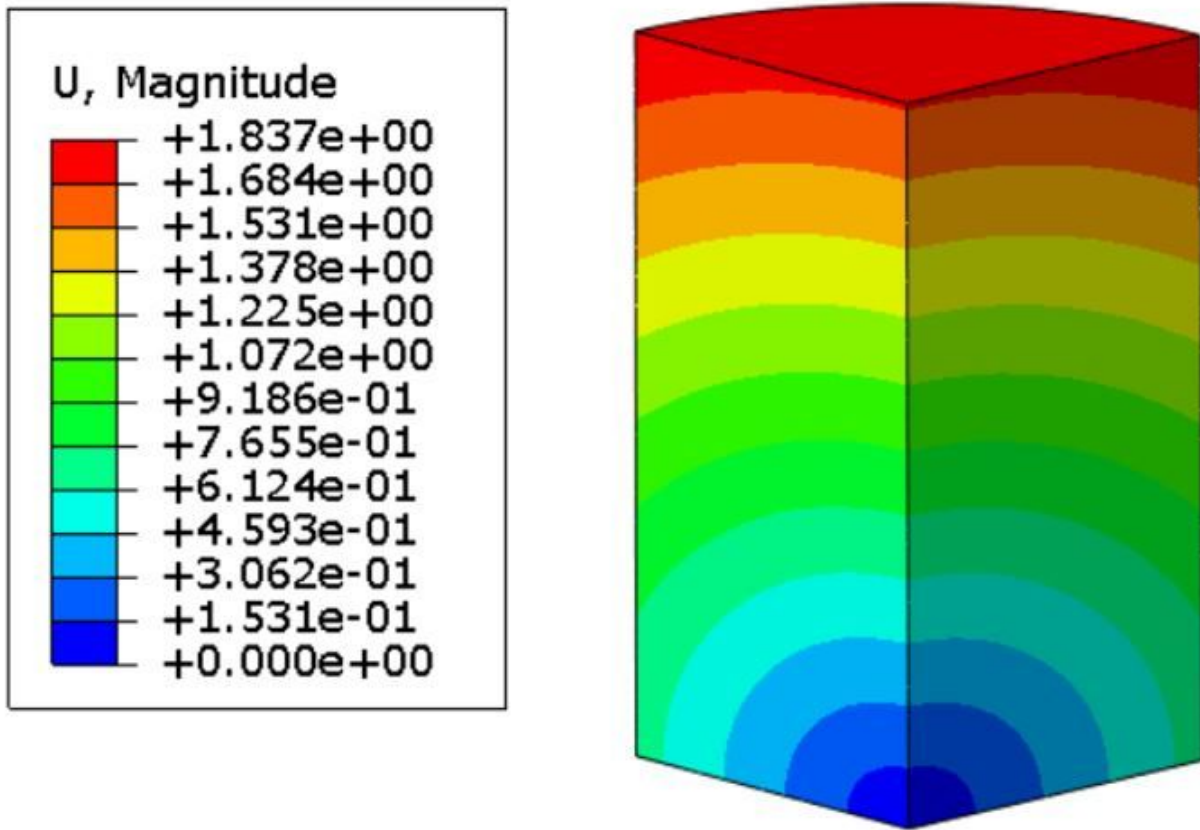


Figure 6

Material displacement (deformation) distribution diagram

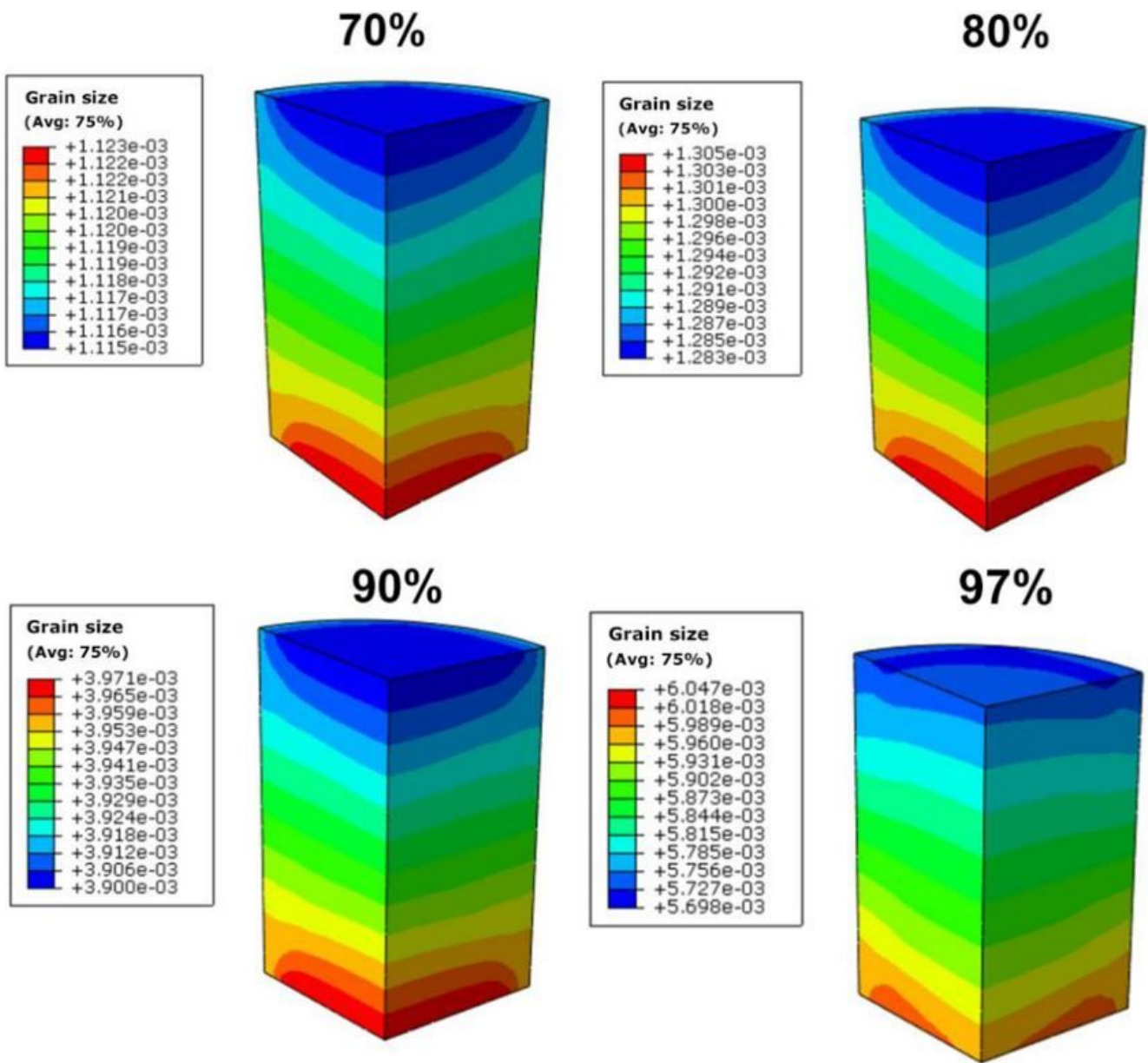
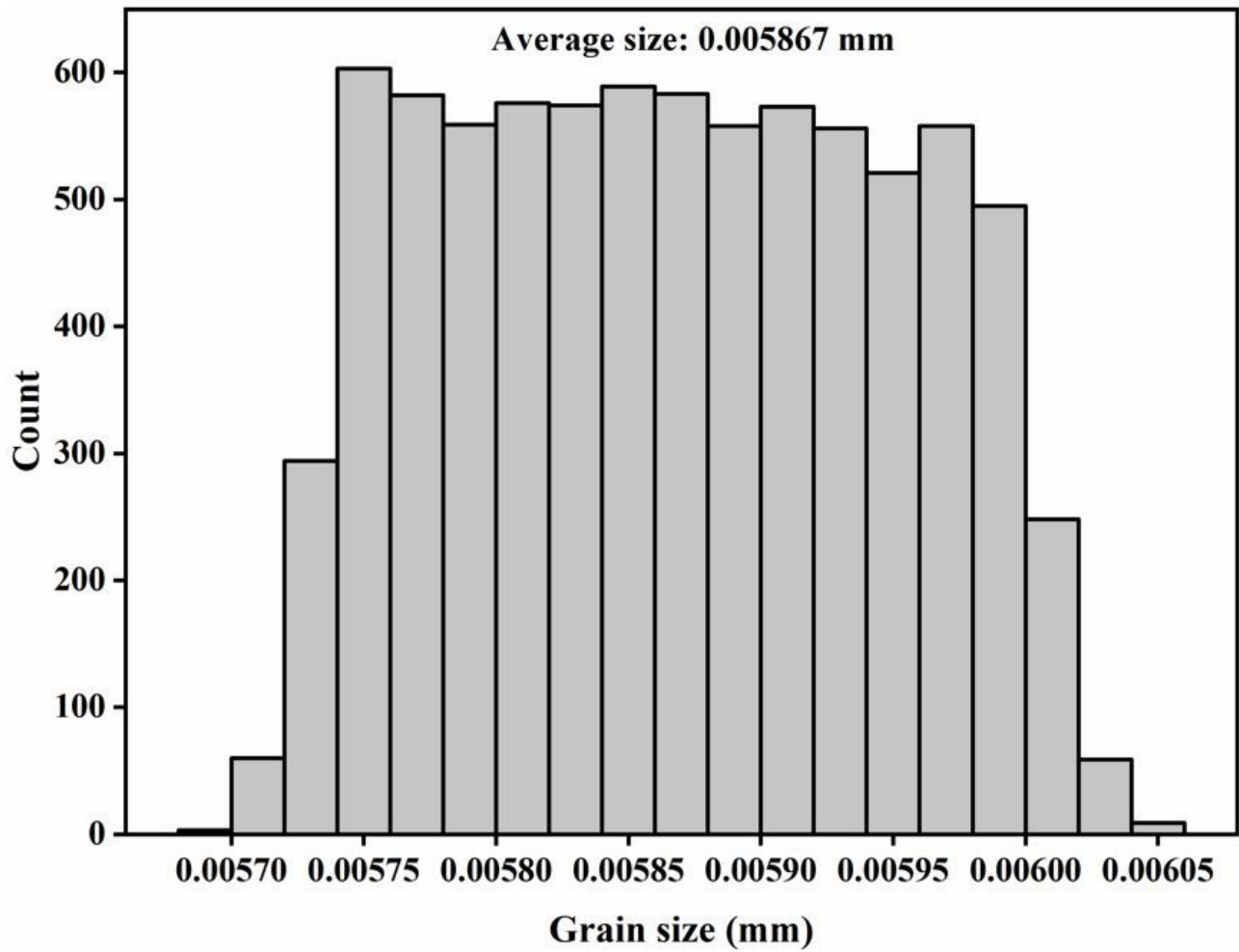


Figure 7

Grain growth diagram



**Figure 8**

Grain size statistics of sintering simulation

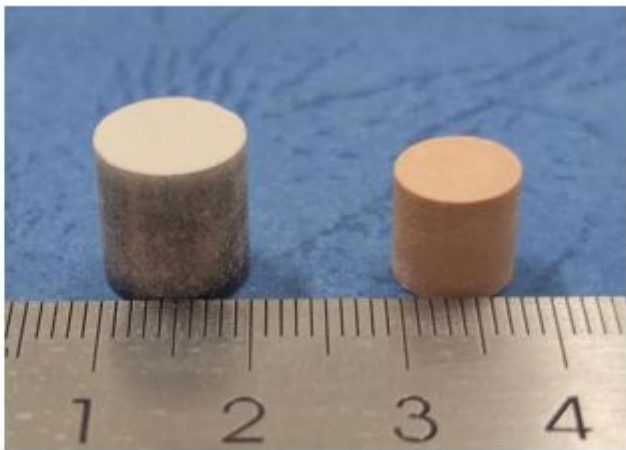


**Figure 9**

Comparison of samples before and after sintering

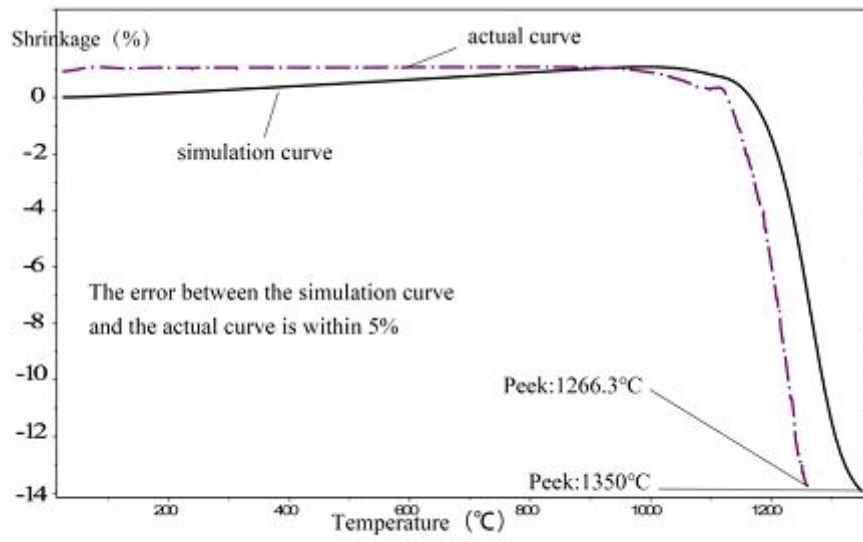


**Figure 10**

Comparison curve of shrinkage change

**Before sintering**

**After sintering**

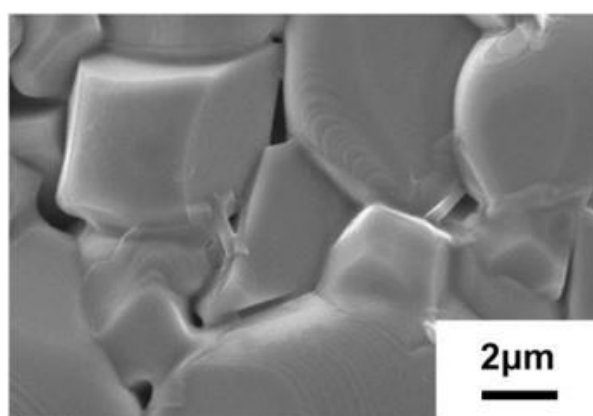
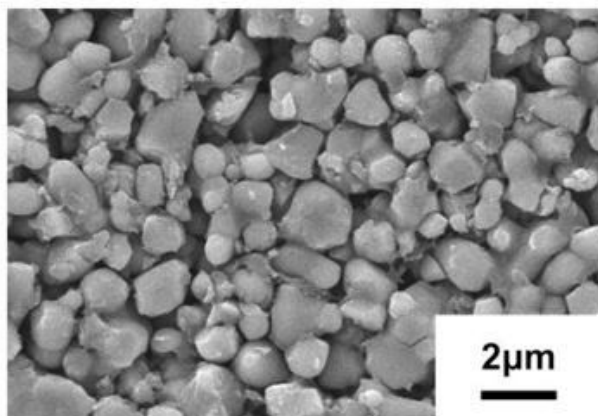
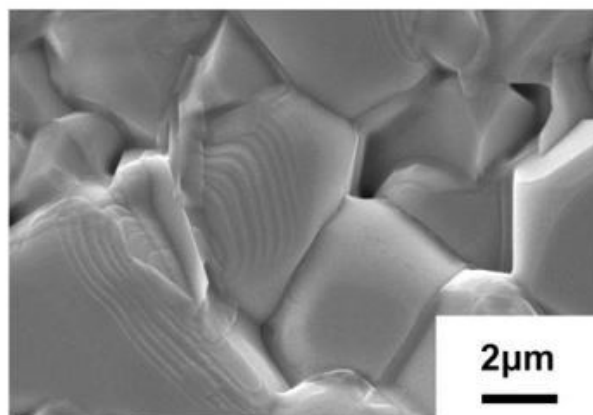
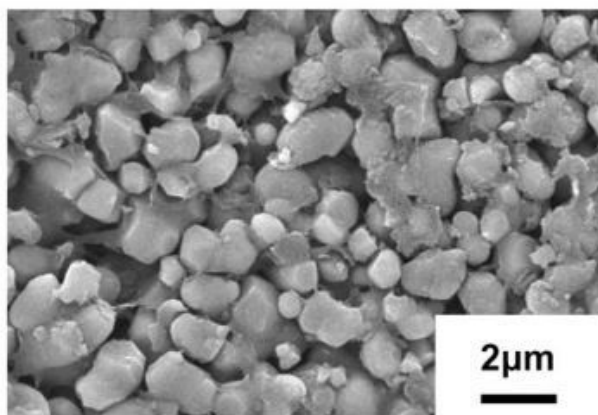
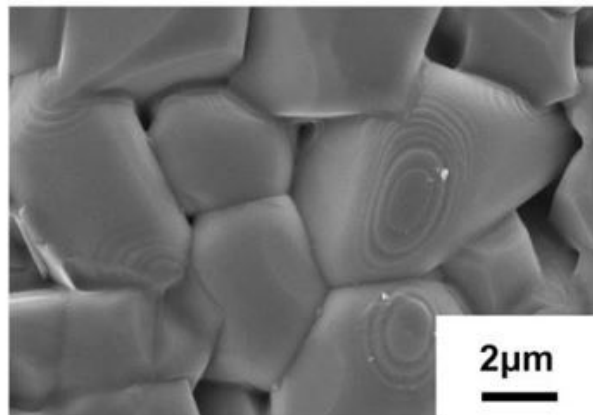
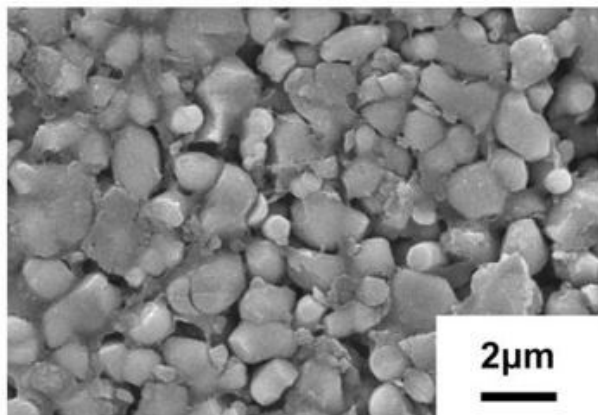
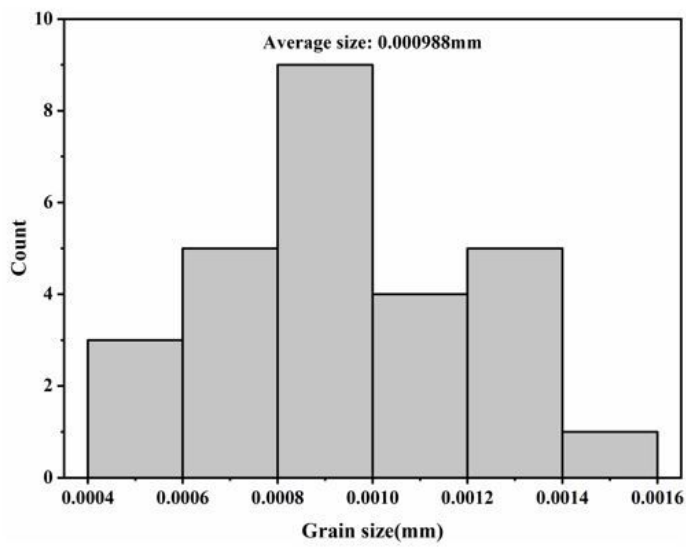
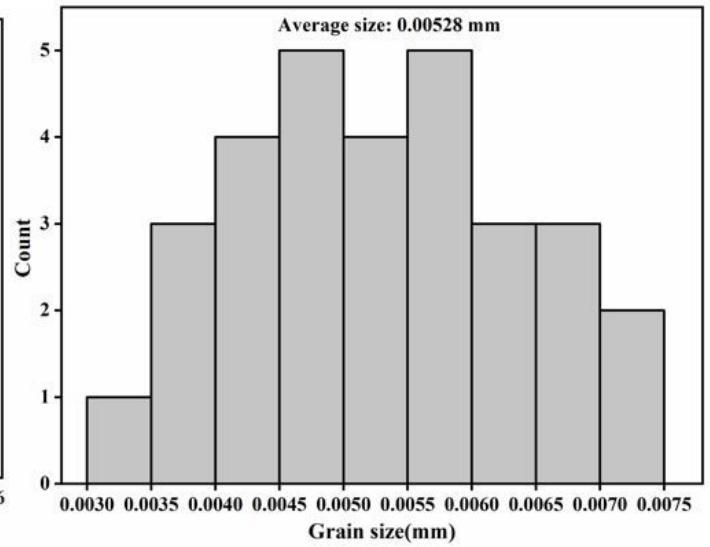


Figure 11

SEM of grain size



(a) Before sintering



(b) After sintering

Figure 12

Grain size statistics of actual sintering

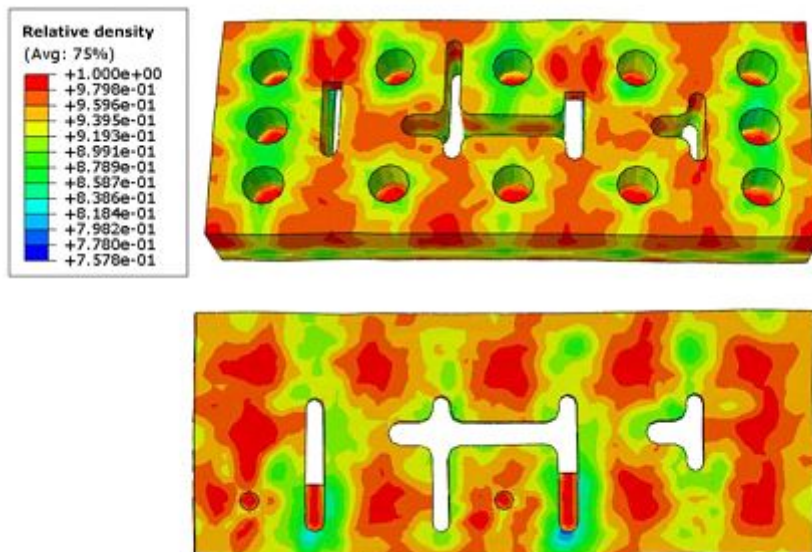


Figure 13

Relative density distribution of filter

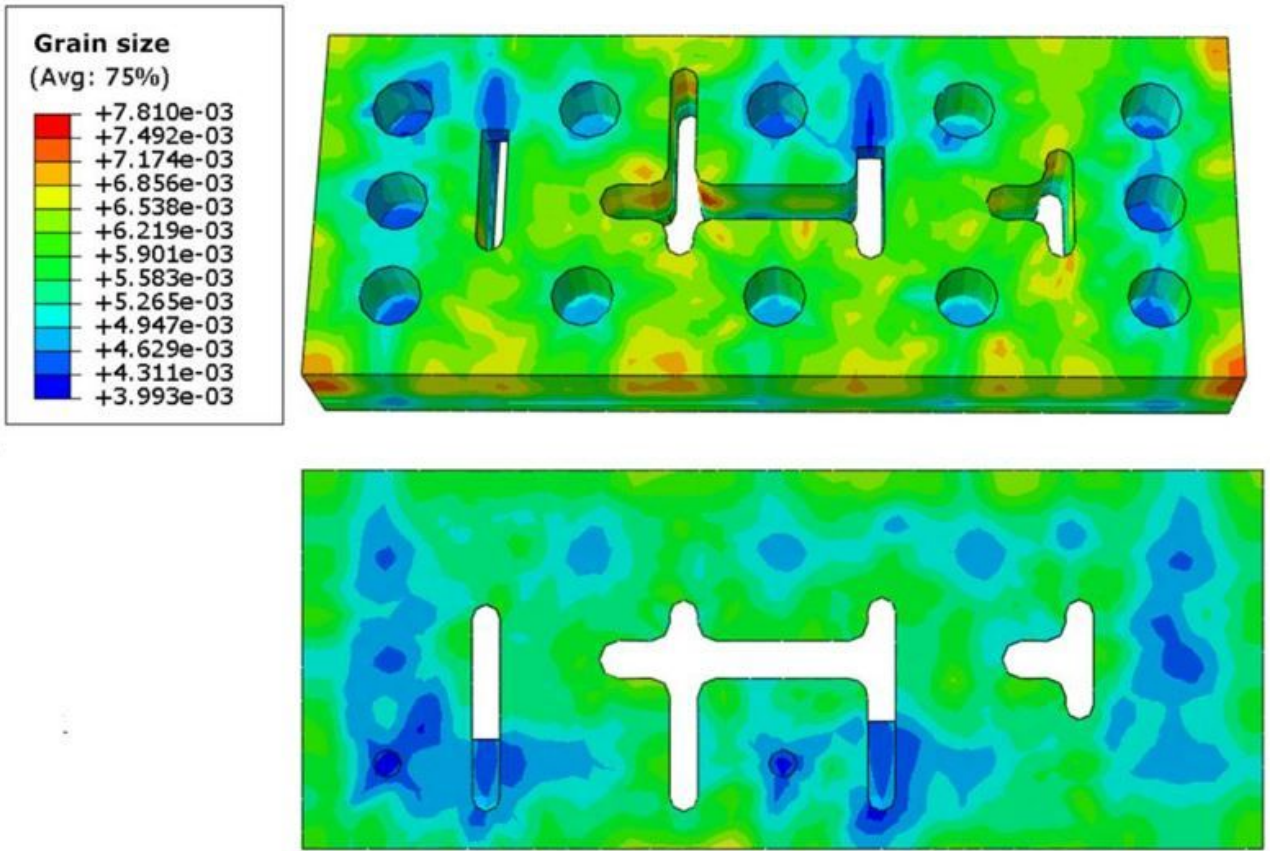


Figure 14

Grain size distribution of filter

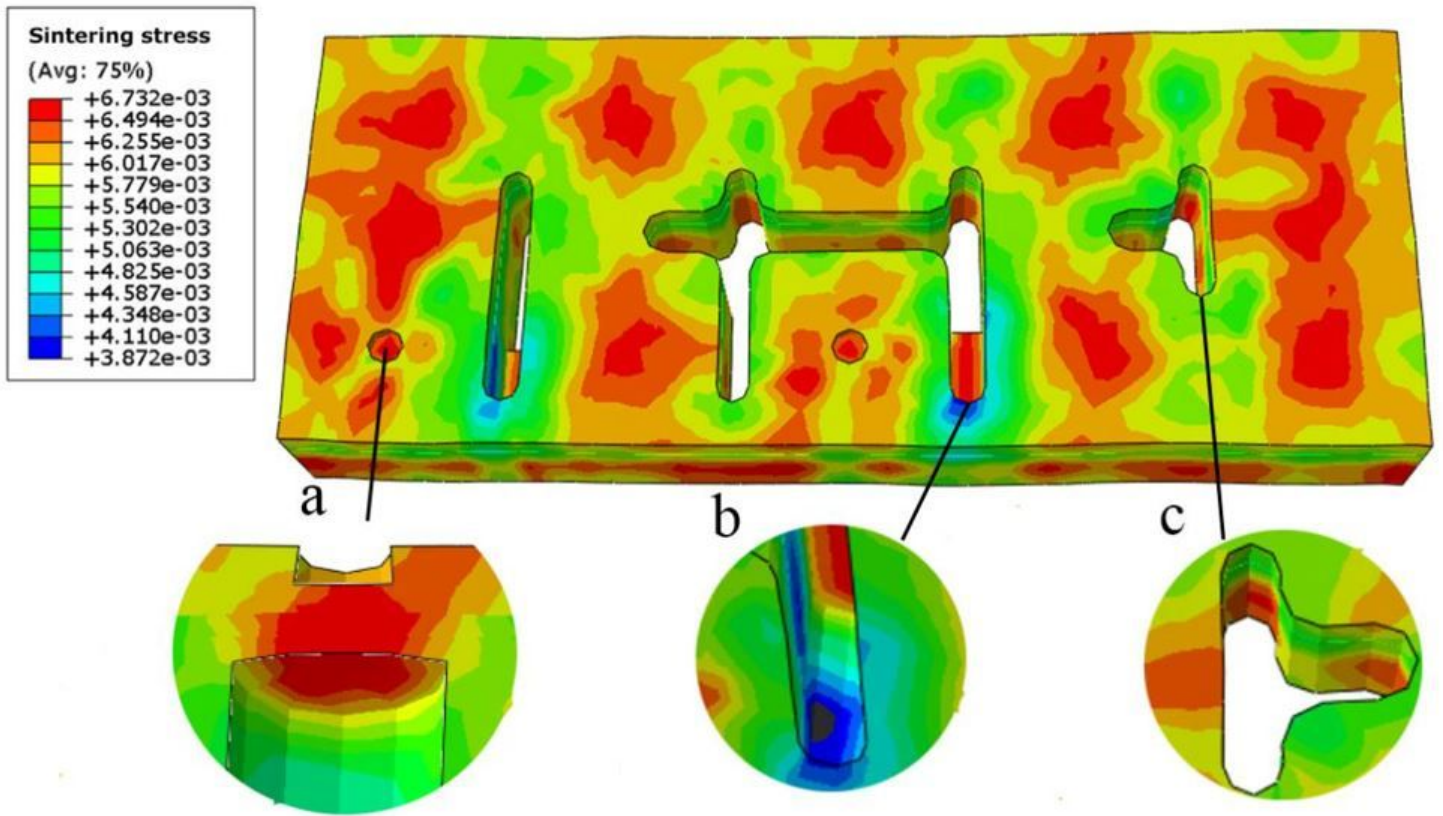
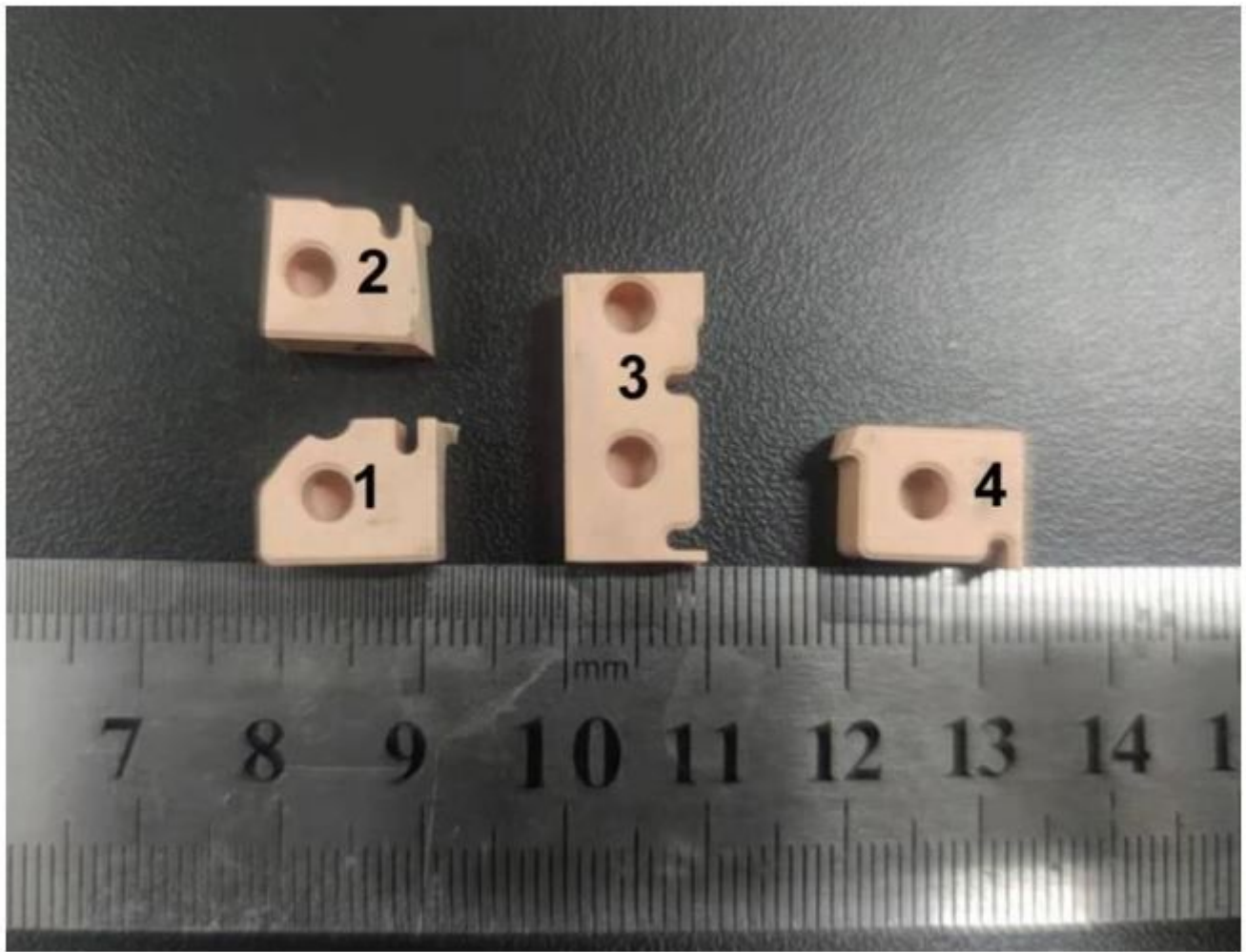


Figure 15

Sintering stress distribution of filter



**Figure 16**

The cut part of sintered part